Vol. 8, No. 3, June 2024, pp. 259-269

Current Optics and Photonics

Regular Paper

# Fabrication of Phase Plate to Simulate Turbulence Effects on an Optical Imaging System in Strong Atmospheric Conditions

**Han-Gyol Oh[1,2], Pilseong Kang[1], Jaehyun Lee[1], Hyug-Gyo Rhee[1,2]*, Young-Sik Ghim[1,2]**, and Jun Ho Lee[3]**

[1]*Korea Research Institute of Standards and Science, Daejeon 34113, Korea*
[2]*Department of Precision Measurement, University of Science and Technology, Daejeon 34113, Korea*
[3]*Kongju National University, Gongju, 32557, Korea*

(Received February 27, 2024 : revised April 16, 2024 : accepted April 16, 2024)

Optical imaging systems that operate through atmospheric pathways often suffer from image degradation, mainly caused by the distortion of light waves due to turbulence in the atmosphere. Adaptive optics technology can be used to correct the image distortion caused by atmospheric disturbances. However, there are challenges in conducting experiments with strong atmospheric conditions. An optical phase plate (OPP) is a device that can simulate real atmospheric conditions in a lab setting. We suggest a novel two-step process to fabricate an OPP capable of simulating the effects of atmospheric turbulence. The proposed fabrication method simplifies the process by eliminating additional activities such as phase-screen design and phase simulation. This enables an efficient and economical fabrication of the OPP. We conducted our analysis using the statistical fluctuations of the refractive index and applied modal expansion using Kolmogorov's theory. The experiment aims to fabricate an OPP with parameters $D/r_0 \approx 30$ and $r_0 \approx 5$ cm. The objective is defined with the strong atmospheric conditions. Finally, we have fabricated an OPP that satisfied the desired objectives. The OPP closely simulate turbulence to real atmospheric conditions.

*Keywords* : Adaptive optics, Air disturbance, Fabrication, Optical phase plate
*OCIS codes* : (010.1330) Atmospheric turbulence; (220.1080) Active or adaptive optics; (220.4610) Optical fabrication

## I. INTRODUCTION

The quality of images observed through telescopes is often compromised by the aberration of light entering from space. This distortion arises when light, emitted by sources such as stars in the form of plane waves, becomes distorted while traversing Earth's atmosphere, resulting in what is known as air disturbance, as shown in Fig. 1(a). This phenomenon not only affects telescopes but also other optical instruments using light that has propagated through the atmosphere, leading to the degradation of image quality and source coherence [1]. To address these challenges, adaptive optics (AO) technology is employed to correct distorted waves, thereby enhancing the performance of optical systems [2]. However, to effectively investigate AO systems, it is essential to reproduce atmospheric behavior in laboratory settings, simulating conditions similar to those found in the actual atmosphere. Over the years, various methods have been developed to simulate the turbulence effect in laboratories as discussed below.

Initially, prevalent methods relied on inducing turbulent motion in heated air and water as media [3]. However,

*Corresponding author: hrhee@kriss.re.kr, ORCID 0000-0003-3614-5909
**Corresponding author: young.ghim@kriss.re.kr, ORCID 0000-0002-4052-4939

Color versions of one or more of the figures in this paper are available online.

limitations arose due to minimal changes in the refractive index with temperature, thus requiring a long optical path length. Additionally, the potential for damage to system components and difficulties in disturbance prevention made the use of heat or water impractical for laboratory settings. The most practical approach to simulate air disturbance appeared with the use of an optical phase plate (OPP). Figure 1(b) illustrates a schematic using OPPs in an optical system as an example. While a deformable mirror (DM) or spatial light modulator (SLM) can serve as turbulence compensation devices, it is important to note that these features can introduce complexities and increase the cost of the experiment [4]. A common method involves simulating turbulence through computer simulations based on the Kolmogorov atmospheric model. This generates a phase screen with a constant Fried parameter ($r_0$) [5]. However, the real atmosphere exhibits variations in the Fried parameter due to turbulence randomness, a characteristic that can't be captured by this method.

Various approaches to fabricating OPPs have been explored. The near-index matching method, creating a sandwich-like structure with materials of similar but not identical refractive indexes, is one example [6]. Diffractive optics, including phase diffusers, molded plastic optics, and computer-generated holograms, have also been employed to simulate air disturbance [7]. Transparent materials, such as multiple layers of hairspray sprayed on glass, have been used to create variations in thickness and produce optical path differences [8, 9]. Researchers have developed phase-screen transmission model algorithms to closely simulate actual atmospheric conditions [10–12].

This paper proposes a novel two-step process for fabricating an OPP that simulates strong turbulence. We use the $D/r_0$, where D represents the telescope diameter and $r_0$ is the Fried parameter, to express the strength of atmospheric turbulence. The Fried parameter, $r_0$, characterizes the coherence length of the wavefront phase distortions due to atmospheric turbulence. Therefore, $D/r_0$ serves as a value of the

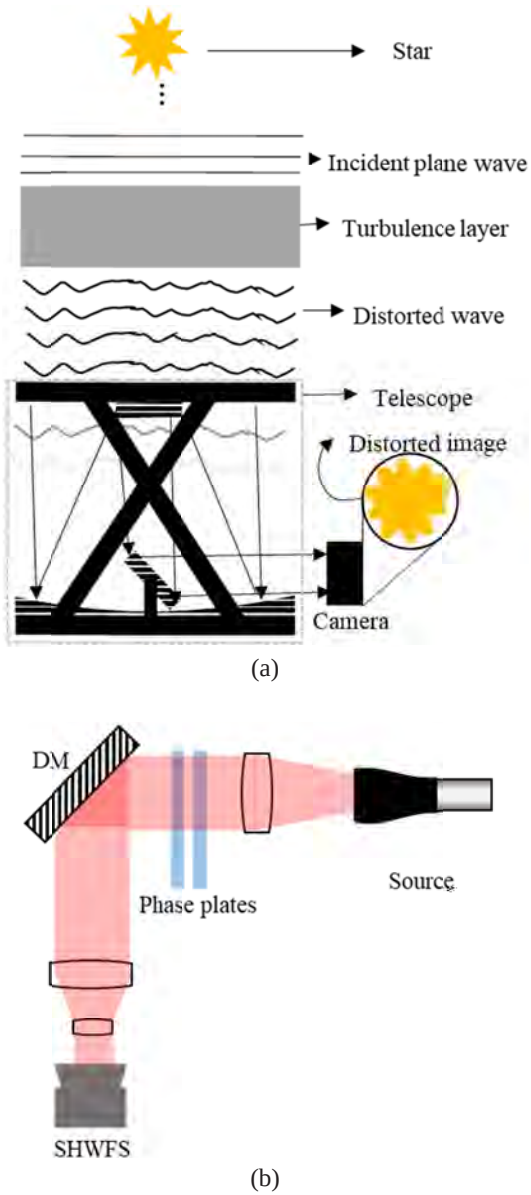


**FIG. 1.** Schematic diagram of (a) effect of turbulence layer (atmosphere) in the telescope, (b) adaptive optics (AO) system using an optical phase plate (OPP) as the turbulence layer.

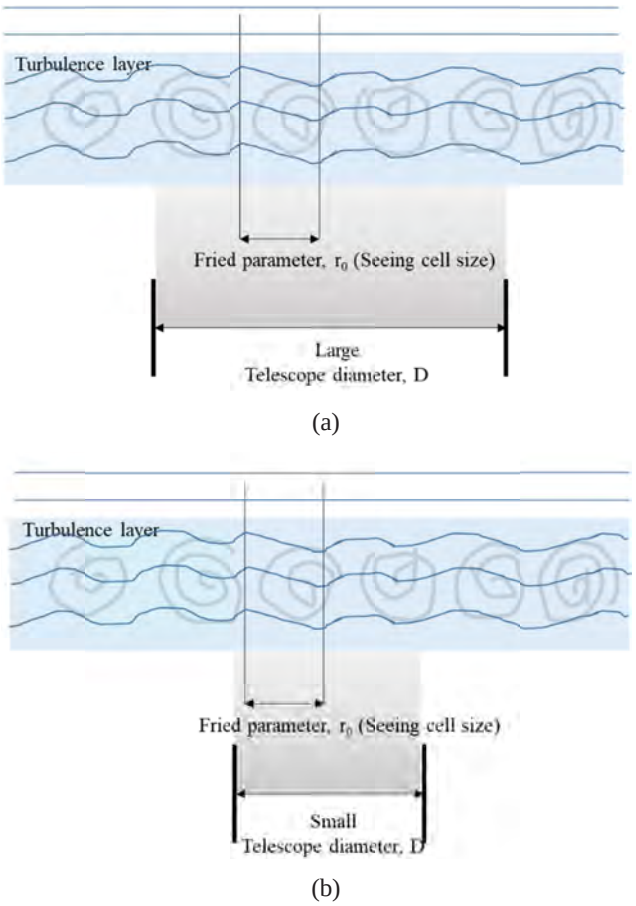


**FIG. 2.** Changes in $D/r_0$ with telescope diameter size: (a) Large, (b) small.

relative strength of turbulence as seen through telescopes of varying diameters. Figure 2 illustrates that with the same Fried parameter, the perceived intensity of turbulence can vary depending on the diameter of the telescope. Therefore, using $D/r_0$ allows us to communicate the relative intensity of turbulence. Considering a moderate turbulent condition with $D/r_0 = 10$, OPP should simulate a higher $D/r_0$ [13]. We assumed the strong turbulent condition level by setting $D/r_0 = 30$–$40$ approximately [14].

The fabrication method relies on material properties without designing a phase screen, making it accessible and cost-effective for anyone with the required materials. This simplifies the fabrication process, which is divided into two parts: The etching-hairspray process and the etching-epoxy resin process. In the etching-hairspray process, hairspray is applied to create variations in thickness, resulting in optical path differences (OPD) and high-order term aberrations. This process effectively simulates actual atmospheric turbulence by introducing random changes that simulate real disturbances. In the etching-epoxy resin process, epoxy resin replaces hairspray to produce high-order term aberrations based on its anisotropic material properties after curing. This process offers the ability to simulate a high level of turbulence. The OPPs are then analyzed using statistics of refractive index fluctuations and modal expansion from Kolmogorov's theory.

Ultimately, the fabricated OPPs closely simulate actual air disturbance by incorporating high-order term aberrations through etching and randomness using material properties [15]. The evaluation of OPPs fabricated with the two methods deems them suitable for high air disturbance, and they are compared with the Fried parameter. Section 2 introduces the principles for analyzing the OPP, Section 3 details the experimental method and results, and Section 4 provides a discussion and summary.

## II. THEORY

### 2.1. Statistics of the Index of Refraction Fluctuations

The body of research on optical propagation through turbulence is vast. However, most of the published literature is rooted in the efforts of Kolmogorov, Tatarskii, and Fried [16]. In this section, we focus on Kolmogorov's work. Kolmogorov developed a statistical model of a spatial structure of turbulent air flows. It is necessary when expressing atmospheric turbulence stati,stically. The statistical distribution, denoted as $\mathbf{\Phi}_n(\vec{\kappa})$, of the size and number of eddies can be specified by the spatial power spectral density of the refractive index $n_1(\vec{r})$, where the variables $\vec{\kappa}$ and $\vec{r}$ represent the spatial wavenumber vector and the three-dimensional position vector, respectively. Kolmogorov's theory predicts that this can be expressed in the form of $\mathbf{\Phi}_n(\vec{\kappa})$. Before introducing the form, it should be noted that the theory has three regimes [17]. For very small $\kappa$, *i.e.*, $\kappa < 2\pi/L_0$, Kolmogorov's theory does not predict a mathematical form of $\mathbf{\Phi}_n(\vec{\kappa})$, where the variable $\kappa$ represents the scalar wavenumber. The quantity $L_0$ represents the characteristic dimension of the largest turbulent eddies. Inhomogeneities larger than $L_0$ are no longer assumed to behave as if they are homogeneous. For a very large $\kappa$, *i.e.*, $\kappa > 2\pi/l_0$, a mathematical form of $\mathbf{\Phi}_n(\vec{\kappa})$ is also not predicted by Kolmogorov's theory. The quantity $l_0$ represents the characteristic dimension of the smallest turbulent eddies. When $\kappa$ is in the range of $2\pi/l_0 \le \kappa \le 2\pi/L_0$, the form of $\mathbf{\Phi}_n(\vec{\kappa})$ is predicted by Kolmogorov's theory. Within this wavenumber range, Kolmogorov's theory finally predicts the form of $\mathbf{\Phi}_n(\vec{\kappa})$ as follows:

$$\Phi_n^K(\vec{\kappa}) = C_n \kappa^{-} \quad . \tag{1}$$

The quantity $C_n^2$ is the structure constant following changes in the refractive index and represents the intensity of a change in the refractive index.

At this point, we introduce the structure function of the random index of a refraction distribution. In systems that create images through atmospheric turbulence, this structure function plays a special role as the structure function of turbulence naturally occurs according to an analysis of a telescope's average optical transfer function. The phase structure function $D_n(\vec{r})$ of the homogeneous refractive index is defined here by Eq. (2).

$$D_n(\vec{r}) = E\left[n(\vec{r}) - n(\vec{r}+\vec{r})\right] \quad . \tag{2}$$

By using the definitions in Eqs. (1) and (2), we obtain the following result:

$$D_n(r) = C_n r \quad , \tag{3}$$

If $\mathbf{n_1}(\vec{r})$ is isotropic, the structure function depends on the scalar variable $r = |\vec{r}|$. Symmetrically, the structure function of the phase can be defined by Eq. (1).

$$D_{\psi_i}(\Delta\vec{x}) = \langle \psi_i(\vec{x}) - \psi_i(\vec{x}+\Delta\vec{x}) \rangle, \tag{4}$$

where $\psi_i(\vec{x})$ is the phase perturbation at the transverse vector location $\vec{x}$.

Fried expressed the phase structure function as a function of the Fried parameter:

$$r_{o_i} = \left[\frac{\pi}{k\, C_{n_i} \Delta z_i}\right] \quad , \tag{5}$$

where the variables k and $\Delta z_i$. represent wavenumber and the thickness of the turbulence layer. The structure constant of the index of refraction fluctuations, $C_n^2$, is used to characterize the strength of the turbulence. $C_n^2$ has been found to vary as a function of the altitude, location and time of day. Several mathematical models have been developed from experimental measurements of $C_n^2$. A commonly used model is the layered model. Because $C_n^2$ varies with the altitude, the model suggests breaking the $C_n^2$ profile into

a finite number of layers. Accordingly, the notation $\Delta z_i$ is used to designate the altitude and thickness of the $i^{th}$ layer. The total thickness of the turbulent layer can be expressed by the integral of the $i^{th}$ layer. In this paper, we assumed that the phase plate represents one of the layers used when obtaining $r_0$ by Eq. (5). The thickness of the phase plate is assigned the value of $\Delta z_i$.

### 2.2. Modal Expansion of Perturbation

In the field of imaging optics, efficiently expressing wavefront aberration involves using sets of orthonormal basis functions [17]. Similarly, when studying turbulence effects, it proves advantageous to conceptualize the turbulence of the optical wavefront as a linear combination of orthonormal basis functions. This approach provides insight into the generation of random aberrations resulting from air disturbance. The general mathematical form of this linear transformation, often referred to as the modal transform, is presented as Eq. (6).

$$\psi\left(\vec{x}\right) \approx \sum_{i=}^{N} a_i f_i\left(\vec{x}\right). \tag{6}$$

In this equation, $f_i\left(\vec{\boldsymbol{x}}\right)$ is the $i^{th}$ functions from the set of orthonormal basis functions. $N$ is the total number of basis functions, and $a_i$ denotes the weight associated with the $i^{th}$ basis function.

Zernike polynomials have been widely studied and used to represent aberrations in imaging optic systems [18]. Equation (6) can be specifically expressed as a linear combination of Zernike polynomials. Following a series of mathematical procedures, the averaged mean square phase error ($\epsilon_N^2\left(Z\right)$) after the removal of the first $N$ Zernike modes can be calculated using the Fried parameter [19, 20].

## III. FABRICATION AND MEASUREMENT

This section details the fabrication process of the OPP and outlines the corresponding experimental results. The objective of the experiment was to create an OPP with a $D/r_0$ ratio of approximately more than 30 with the aim to simulate air disturbance in a laboratory environment that closely simulates actual atmospheric conditions, where D represents the pupil diameter of the telescope used, as depicted in Fig. 1(a).

The fabrication of the OPP involved employing an etching, spraying, and epoxy resin process. After numerous iterations and clarification through trial and error, a successful methodology for producing the OPP was established.

Before beginning the experiment, careful consideration was given to selecting the measuring instrument for observing the results of each process. The chosen instrument for this study was the Shack-Hartmann wavefront sensor (SHWFS). While an interferometer was initially considered as the measuring instrument, its limitations became apparent during the manufacturing process, specifically when the Fried parameter ($r_0$) of the OPP was reduced. The interferometer exhibited a significant data drop that interrupted thorough analysis. Consequently, the SHWFS was adopted for its capability to capture a broad range of measurements, particularly those involving high slopes and wavefronts with substantial deformations.

Despite the SHWFS having structural limitations that render it less accurate and lower in resolution compared to the interferometer, cross-checking with an interferometer confirmed that the targeted $r_0$ level was unaffected. The cross-checking method is shown in Figs. 3(a) and 3(b). Measurements were obtained by a commercial 300 mm Zygo interferometer and the SHWFS (WFS40-14AR; Thorlabs Inc., NJ, USA) [21]. The results, displayed in Fig. 3(c), showed minimal differences with a 2 nm root-mean-square (RMS) value and an $r_0$ of 3.5 mm for both instruments. Based on these findings, the decision was made to use the

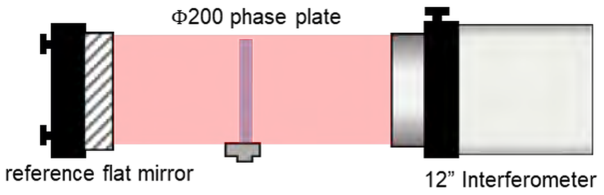


(a)

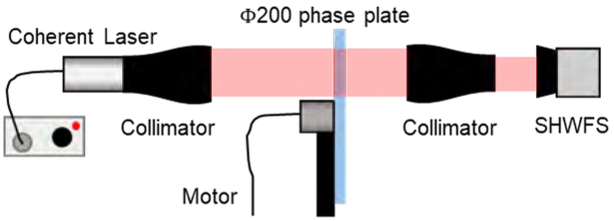


(b)

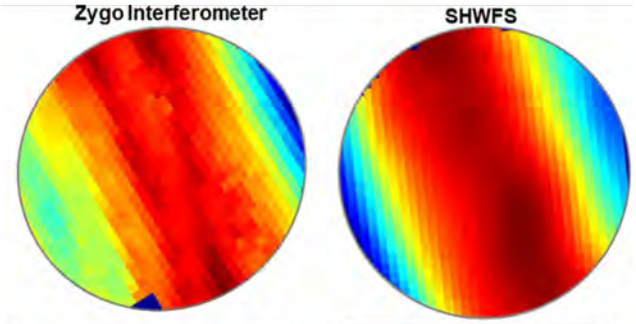


| | |
|---|---|
| PV | 0.169 μm |
| RMS | 0.032 μm |
| $r_0$ | 39.8 mm |

| | |
|---|---|
| PV | 0.132 μm |
| RMS | 0.032 μm |
| $r_0$ | 36.3 mm |

(c)

**FIG. 3.** Schematic diagram of transmission wavefront measurement by (a) an interferometer and (b) a Shack-Hartmann wavefront sensor (SHWFS); (c) Cross-check data by those instruments at the same location.

SHWFS instead of the interferometer.

Moreover, the SHWFS can accommodate a circular aperture of up to 11.26 mm in diameter when capturing a single-shot image. However, this proved insufficient for obtaining comprehensive surface data. To overcome this limitation, a collimator was employed to increase the effective pupil size to 20 mm (full size = 30 mm, with a margin of 5 mm from the side). The measurement system is depicted in Fig. 3(b), where 12 shots were captured at different locations on a 200-mm-diameter OPP. Consequently, 12 transmission wavefronts were obtained for a single OPP, as illustrated in Fig. 4 for clarification.

### 3.1. Fabrication Process 1: Etching

To estimate the impact of etching, seven glass plates with a 200 mm diameter each were prepared and named Plate 1 to 7. Hydrofluoric acid etching was conducted on these lapped glass plates without a predefined phase screen. A transmission wavefront, illustrating the optical quality of the initial OPP, was randomly generated. The glass plates underwent etching without any pretreatment, with each of the seven plates being etched in minute increments ranging from 1 min to 7 min.

An upper limit of 7 min was set due to the interferometer's inability to measure the plate etched for 4 min. To address this limitation, a range of 3 min above and below the 4-min mark was established. The results of the experiment showed that longer etching times resulted in a higher ratio of Zernike high-order aberrations. However, for the plate etched for 7 min, data acquisition from the SHWFS was not possible due to excessively high wavefront deformation.

Following the experimental procedures, we used the Karhunen-Loeve expansion to analyze the data from the OPP [16]. This statistical method provides an optimal basis for modeling the phase of a turbulence-corrupted wavefront. With this approach, we made a Zernike-Kolmogorov (ZK) residual error graph to verify whether the wavefront through OPP fabricated by the randomness of the material adhered to the modeled turbulence wavefront.

The ZK graph comparing the initial plate with the etched plates showed a notable increase in the ratio of Zernike high-order modes for all plates except the one etched for 1 min. Figure 5 demonstrates this trend, indicating that the initial plate before etching had a small ratio of high-order modes, as depicted in Fig. 6. Consequently, the ZK graph follows the etching pattern for 1 min.

Following the determination of optimal conditions based

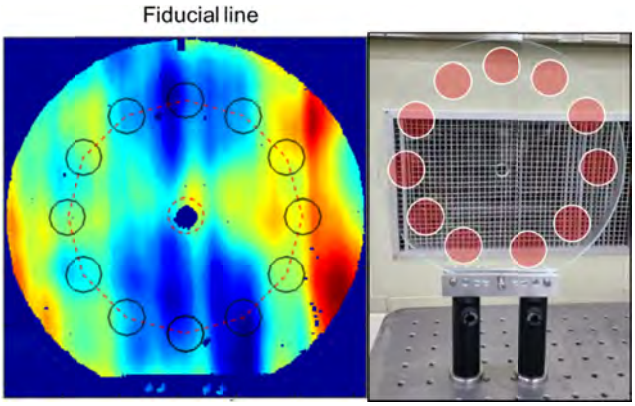


**FIG. 4.** Locations chosen for measurement using a commercial Fizeau interferometer.

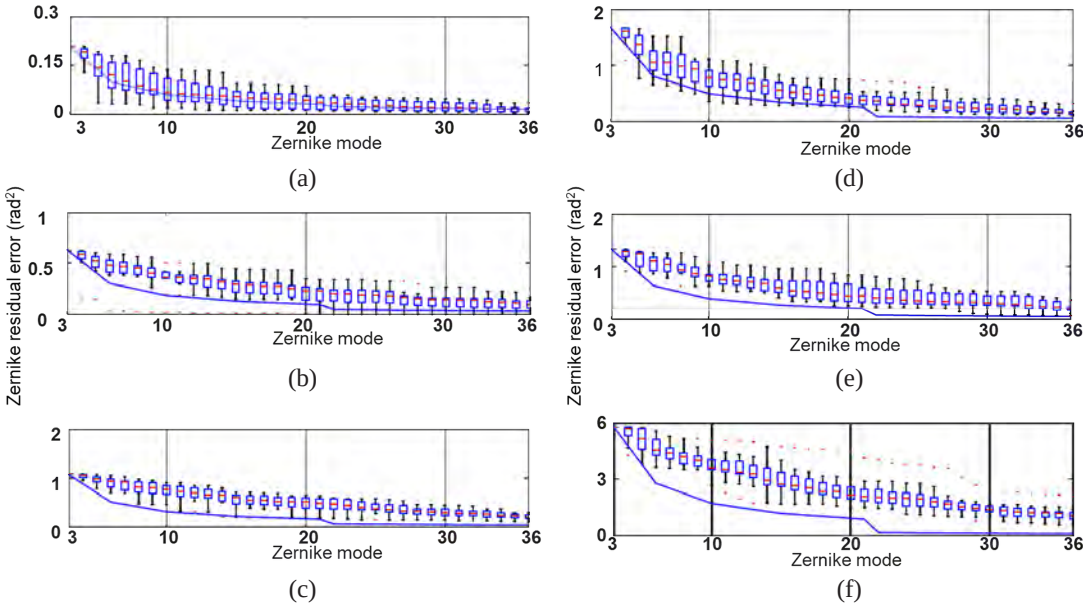


**FIG. 5.** Zernike-Kolmogorov (ZK) graph after etching: (a) Plate 1 (1 min), (b) plate 2 (2 min), (c) plate 3 (3 min), (d) plate 4 (4 min), (e) plate 5 (5 min), and (f) plate 6 (6 min). The Modeled wavefront is described as a blue solid line based on the Karhunen-Loeve expansion. Experimental data are presented in the form of a box plot.

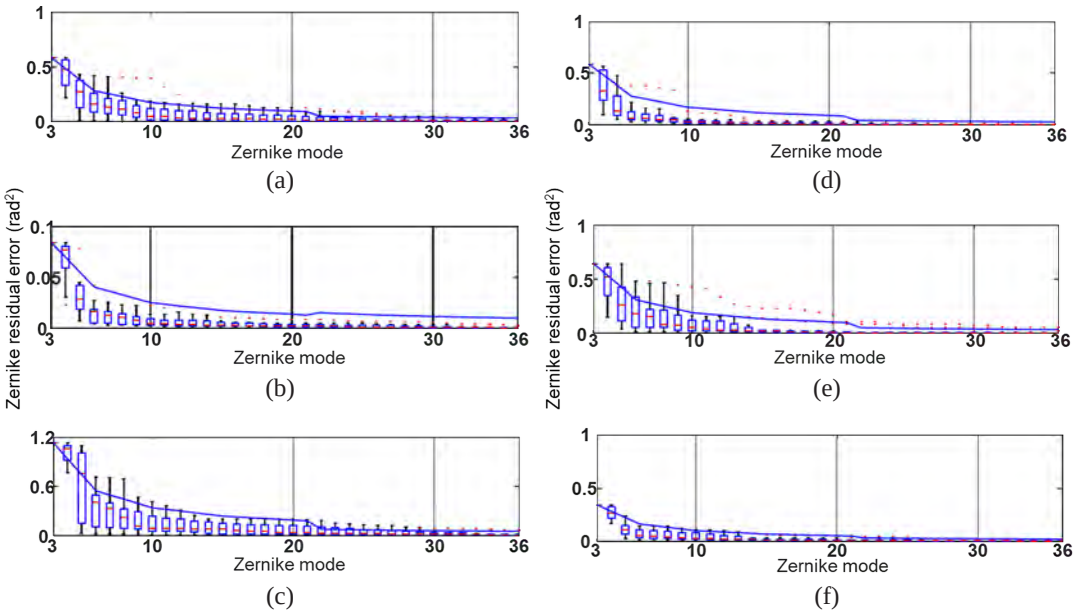


**FIG. 6.** Zernike-Kolmogorov (ZK) graph before etching: (a) Plate 1, (b) plate 2, (c) plate 3, (d) plate 4, (e) plate 5, and (f) plate 6. The Modeled wavefront is described as a blue solid line based on the Karhunen-Loeve expansion. Experimental data are presented in the form of a box plot.

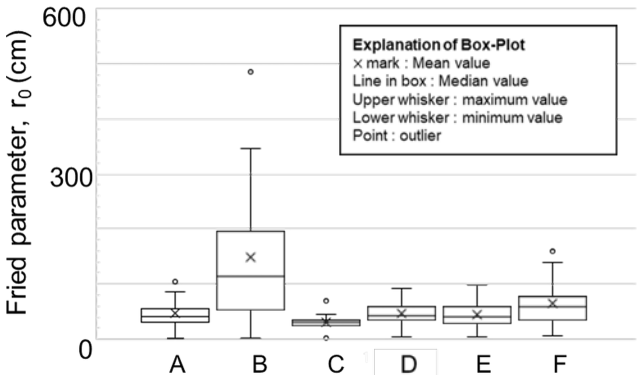


**FIG. 7.** Box plot for the distributed range of the initial $r_0$.

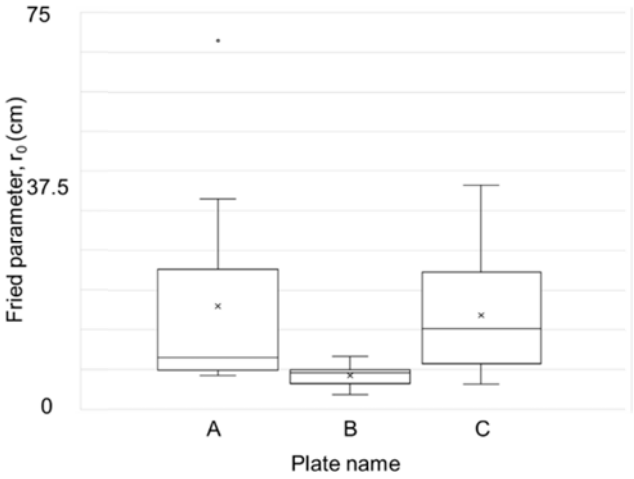


**FIG. 8.** Distributed range of the $r_0$ after spraying.

on the results above, six-phase plates were prepared with a 1 min etching time and labeled as plates A to F. Three of these plates were treated with acrylic spray, while the remaining three were stacked with epoxy resin. The production of six OPPs was completed. Figure 7 presents a boxplot of $r_0$ for the 12 locations on the initial plates.

### 3.2. Fabrication Process 2-1: Acrylic Spraying

Following the etching process, we proceeded with the next step, which involved the application of Krylon acrylic spray [9]. This spray was applied to the surfaces of etched plates named plate A, B, and C, each having undergone a 1 min, and etching process as mentioned previously. The spraying was conducted in an environment resembling a laboratory setting. The acrylic spray was evenly applied by hand on a horizontally placed table for approximately 10 seconds to ensure a thorough and uniform coating across the plate's surface.

A boxplot illustrating the $r_0$ values for the 12 locations on the sprayed plates is presented in Fig. 8. Overall, the mean $r_0$ value for the OPPs after spraying remained around mean $r_0$ = 14.57 cm, with a $D/r_0$ ratio generally averaging 10.29. The ZK residual error after spraying was comparable to the state before spraying, indicating that the spraying process did not significantly affect the Zernike aberration changes on the surface. A ZK residual error graph post-spraying is depicted in Fig. 9.

### 3.3. Fabrication Process 2-2: Stacking Epoxy Resin

Our second proposed method involves stacking epoxy resin onto the previously etched OPP. Specifically, Artglory

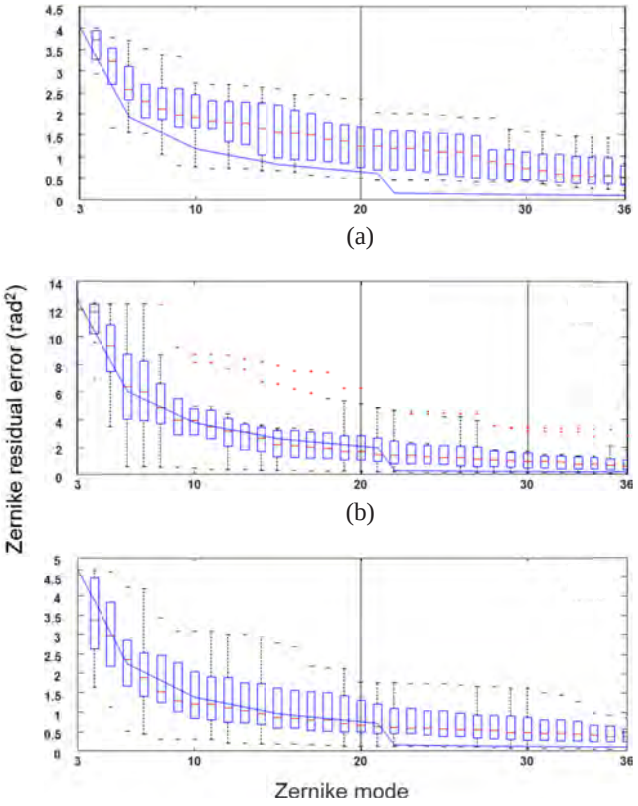


(a)

(b)

(c)

**FIG. 9.** Zernike-Kolmogorov (ZK) graph after spraying: (a) Plate A, (b) plate B, and (c) plate C. Modeled wavefront described as a blue solid line based on the Karhunen-Loeve expansion. Experimental data are presented in the form of a box plot.

31 epoxy resin [22], mixed in a 3:1 ratio with the subject and curing agent, was applied to three etched plates (D, E, F). The resin was then allowed to cure at 23 °C for 24 hours. To prevent the resin from flowing down during the stacking process, a frame was bonded to the etched OPP before pouring the epoxy resin. Figure 10 illustrates the process of stacking epoxy resin onto the glass plate with the bonded frame.

The epoxy resin with 32 g was selected to have a 2-mm thickness based on some experiments. Figure 11 shows the averaged phase maps of 12 locations corresponding to each thickness of resin.

The outcome of the experiment to determine the appropriate thickness is depicted in Fig. 11. When the OPP was measured with the SHWFS, a data drop was observed for thicknesses exceeding 4 mm. Extrapolated data is presented in Fig. 11(d). Thicknesses below 1 mm resulted in non-random phase patterns due to a high proportion of spherical aberration in each location. Consequently, a thickness of 2 mm was expected to be suitable.

A boxplot illustrating the $r_0$ values for the 12 locations on the epoxy resin plates is shown in Fig. 12. After curing, the mean $r_0$ value for the OPPs remained around $r_0$ = 3.58 cm, with a $D/r_0$ ratio generally averaging 41.90. It was challenging to achieve a smaller $r_0$ in our case. The ZK residual error after curing the epoxy resin is depicted in Fig. 13. Similar to the spraying process, curing did not significantly affect the Zernike aberration changes. The mean $r_0$ for each process step is summarized in Table 1.

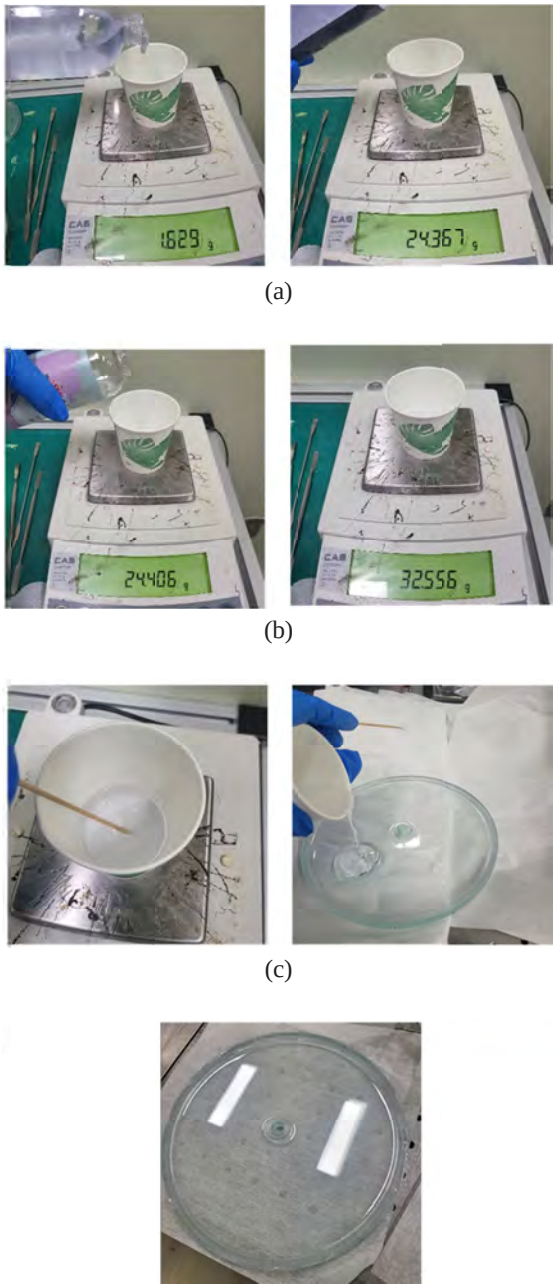


(a)

(b)

(c)

(d)

**FIG. 10.** The process of stacking epoxy resin: (a) Pour the subject of resin (24 g), (b) pour the curing agent of resin (8 g), (c) mixing the subject and curing agent, and (d) curing.

## IV. RESULTS AND DISCUSSION

Our objective was to create an OPP that could simulate air disturbance simulating real atmospheric conditions with

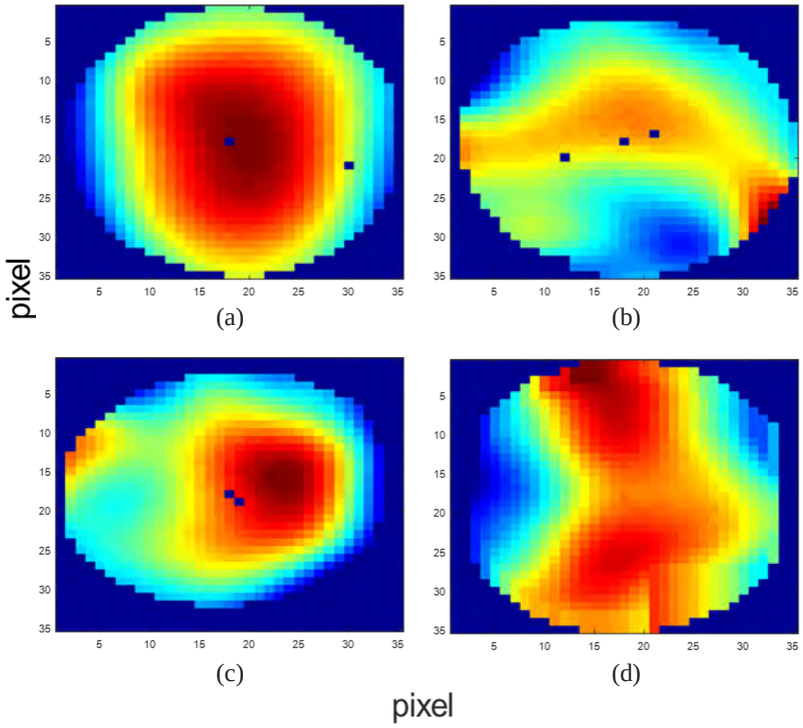


**FIG. 11.** Averaged phase map of 12 locations corresponding to each thickness of epoxy resin: (a) 1 mm, (b) 2 mm, (c) 3 mm, and (d) 4 mm (extrapolated data), respectively. Several blank points in each figure are missing data.

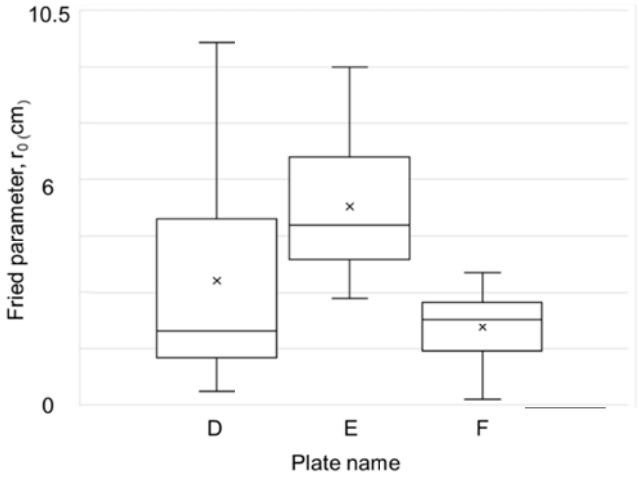


**FIG. 12.** Distributed range of the $r_0$ after stacking epoxy resin.

a $D/r_0$ level of over 30 and $r_0$ around 5 cm. To achieve this, we aimed to produce an OPP that follows the ZK residual error graph. As the 1 min etching process was found to generate aberrations aligning with the ZK graph, three new plates were generated for both the spraying and epoxy resin stacking methods and denoted as plates A to F.

For the final results, the $r_0$ value of the OPP was obtained as the average value for 12 locations. This approach aligns with real atmospheric measurements, where the average $r_0$ value over a specific time range is considered [23]. The analysis results for each of the three manufactured

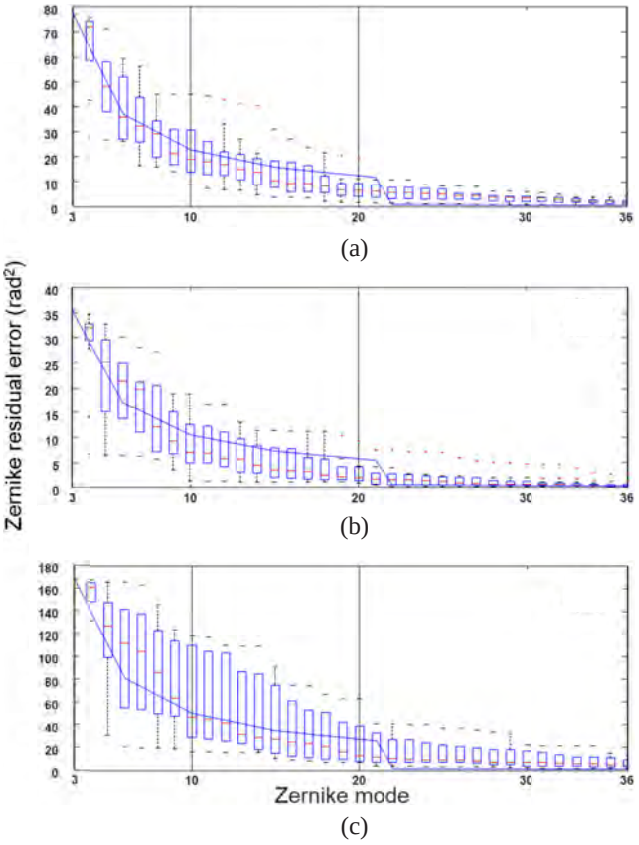


**FIG. 13.** Zernike-Kolmogorov (ZK) graph after spraying: (a) Plate D, (b) plate E, and (c) plate F. The Modeled wavefront is described as a blue solid line based on the Karhunen-Loeve expansion. Experimental data are presented in the form of a box plot.

**TABLE 1.** Average $r_0$ of each process

| Plate Index | Average $r_0$ (cm) | | | |
|---|---|---|---|---|
| | Initial | Etching | Hairspray | Epoxy Resin |
| A | 50.4 | 93.9 | 15.9 | - |
| B | 160.8 | 48.2 | 5.2 | - |
| C | 34.0 | 34.9 | 14.5 | - |
| D | 50.2 | 26.8 | - | 3.3 |
| E | 47.7 | 30.9 | - | 5.3 |
| F | 49.9 | 35.3 | - | 2.1 |

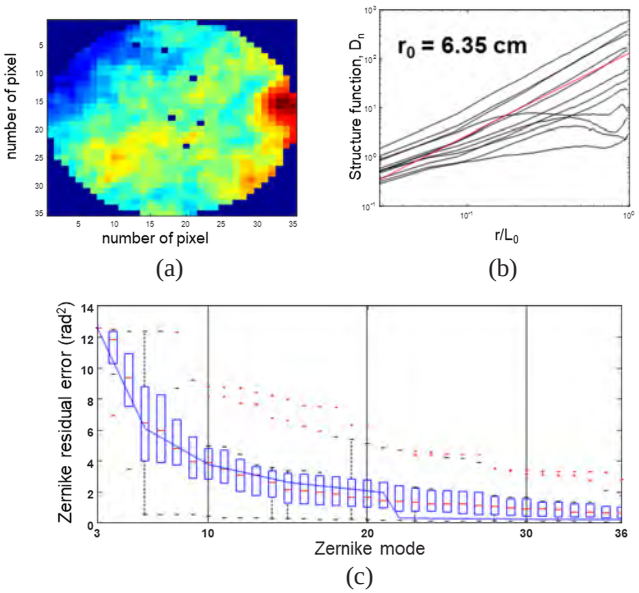


**FIG. 14.** Plate B with the $r_0$ close to $D/r_0$ = 24 in the etching-spraying process. (a) Averaged phase map of 12 locations of plate B measured by Shack-Hartmann wavefront sensor (SHWFS), (b) structure function for 12 locations, where the red line represents the Kolmogorov theory when $r_0$ = 6.35 cm, and (c) Zernike-Kolmogorov residual error graph of plate B.

OPPs are presented for both the etching-spray and etching-epoxy resin methods in Figs. 14 and 15, respectively. The corresponding graphs for Figs. 14(b) and 15(b) represent the structure function for the 12 locations, with the red dotted line indicating the Kolmogorov theory for the average $r_0$ of the OPPs. These figures show variations in $r_0$ around the mean $r_0$ within one OPP, reflecting the expected rotation of the manufactured OPP when mounted and tested in an AO system. This simulation mirrors the real atmosphere's temporal variations in $r_0$ [24, 25].

In the etching-spraying process, plate B exhibited an $r_0$ close to $D/r_0$ = 24, with a final mean $r_0$ of 6.35 cm at a wavelength of 532 nm. Variations in $r_0$ ranged between 2.7 cm and 9.9 cm across the 12 locations. Figure 14 illustrates the results for Plate B.

In the etching-epoxy resin process, plate E exhibited an

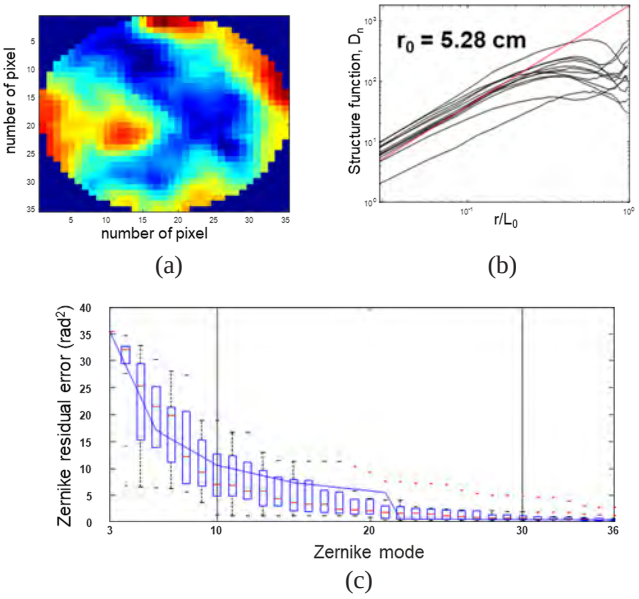


**FIG. 15.** Plate E with the $r_0$ close to $D/r_0$ = 28 in the etching-resin process: (a) Averaged phase map of 12 locations of plate E measured by Shack-Hartmann wavefront sensor (SHWFS), (b) structure function for 12 locations, where the red line represents the Kolmogorov theory when $r_0$ = 5.28 cm, and (c) Zernike-Kolmogorov residual error graph of plate E.

**TABLE 2.** Individual $r_0$ value corresponds to 12 locations

| Location | Average $r_0$ (cm) | |
|---|---|---|
| | Plate B | Plate E |
| 1 | 4.6 | 6.6 |
| 2 | 4.5 | 6.9 |
| 3 | 2.8 | 6.7 |
| 4 | 4.4 | 4.6 |
| 5 | 5.4 | 6.9 |
| 6 | 6.0 | 5.4 |
| 7 | 7.4 | 2.7 |
| 8 | 4.9 | 8.2 |
| 9 | 3.5 | 7.2 |
| 10 | 9.0 | 7.4 |
| 11 | 3.7 | 9.9 |
| 12 | 6.8 | 3.3 |

**TABLE 3.** $r_0$ for two combinations of fabricated four optical phase plates (OPPs) (plates A, B, C, and D)

| P1 | P2 | Average $r_0$ (cm) | D/$r_0$ |
|---|---|---|---|
| A | B | 5.8 | 25.5 |
| A | C | 8.4 | 25.4 |
| A | D | 3.6 | 41.6 |
| B | C | 5.9 | 18.8 |
| B | D | 3.0 | 49.2 |
| C | D | 3.7 | 40.5 |

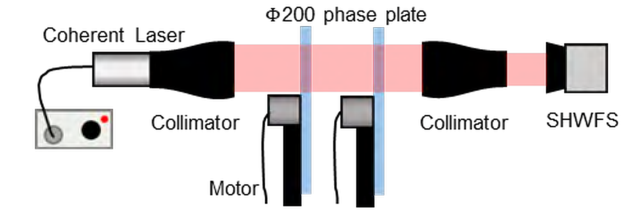


(a)

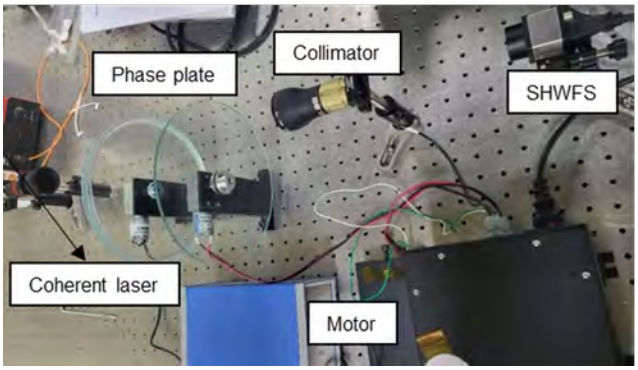


(b)

**FIG. 16.** Measuring two optical phase plates (OPPs): (a) Schematic diagram of the measurement of the $r_0$ with a combination of two OPPs, (b) the optical system with two OPPs.

$r_0$ close to $D/r_0 = 28$. The results for plate E are presented in Fig. 15, indicating a final mean $r_0$ of 5.28 cm, with variations distributed between 2.84 cm and 9 cm, comparable to the conditions of plate B. Individual $r_0$ values for each location of plates A to F are detailed in Table 2.

When the OPP is integrated into an optical system, a combination of two OPPs is employed to enhance randomness. Consequently, two combinations of OPPs, plates A, B, C, and E, were measured. Plates D and F were excluded due to their low $r_0$. Ultimately, the selected combination approached the desired approximately $D/r_0 = 30$–$40$. The average $r_0$ of this combination is presented in Table 3. Figure 16 illustrates the schematic and optical system used for measuring two OPPs, considering an average data scenario from 12 by 12 cases, each incorporating the combination of 12 location data instances for each OPP.

In conclusion, our efforts resulted in the creation of an OPP capable of simulating real atmospheric conditions with a $D/r_0$ level of 30–40, which aligned with the ZK residual error graph. Furthermore, by stacking epoxy resin, we were able to attain a lower $r_0$ value, reaching $D/r_0 \approx 40$.

## V. CONCLUSION

This paper introduces a novel method for fabricating an OPP capable of simulating actual atmospheric turbulence under strong conditions, targeting a $D/r_0$ ratio of 30–40. The fabrication process involves etching, hairspray, and epoxy resin. The etching process creates distortions on the OPP that simulate the features of a turbulent atmosphere based on statistical modeling by Kolmogorov. Hairspray and epoxy resin are employed to modify the Fried parameter ($r_0$) by stacking on the OPP. This approach simplifies fabrication and reduces time and cost by avoiding existing demands for screen design and machining. Experimental measurements and analyses were conducted for both processes using an SHWFS instead of an interferometer.

The proposed fabrication method eliminates the need for additional activities such as designing a phase screen, considering material properties or assessing optical surface quality. The thickness variation of the hairspray and the anisotropic properties of epoxy resin are used to introduce random changes to the OPD. This simplicity and cost-effectiveness make the proposed method advantageous for widespread OPP production. Both processes successfully simulate actual air disturbance by introducing high-order term aberrations through the etching process. The distinction between the two lies in the epoxy resin's ability to simulate a Fried parameter four times lower than that achieved with hairspray. If a significantly lower $r_0$ under $D/r_0 = 40$ is desired, the epoxy resin process is deemed suitable, while the spraying process is recommended for achieving a relatively lower $r_0$ within $D/r_0 = 30$ or less.

However, several considerations must be taken into account during fabrication. The randomness introduced by spray and resin does not align with software predictions. Thus, it is advisable to manufacture the OPP after securing multiple initial plates. Additionally, when using acrylic spray, the temperature during spraying should match that of the storage location to prevent frost formation and water-related issues on the OPP surface. Future work involves applying the fabricated phase plate to experiments with an actual AO system. Further development aims to refine each process to enhance the similarity of the fabricated phase plate to actual atmospheric conditions.

## FUNDING

The authors received no financial support for the research, authorship, and publication of this article.

## DISCLOSURES

The authors declare no conflicts of interest.

## DATA AVAILABILITY

All data generated or analyzed during this study are included in this published article.

## REFERENCES

1. M. Chen, C. Liu, and H. Xian, "Experimental demonstration of single-mode fiber coupling over relatively strong turbulence with adaptive optics," Appl. Opt. **54**, 8722–8726 (2015).

2. P. Kang, J. Huh, K. Lee, S. Park, and H.-G. Rhee, "Design of a discrete flexure for SiC deformable mirror with PMN stacked-actuators," Opt. Express **29**, 31778–31759 (2021).
3. T. A. Rhoadarmer and J. R. P. Angel, "Low-cost, broadband static phase plate for generating atmosphericlike turbulence," Appl. Opt. **40**, 2946–2955 (2001).
4. T. Xu, Y. Li, W. Du, C. Ma, S. Cai, M. Lan, J. Wu, S. Yu, and J. Lin, "Simulating atmospheric turbulence using a spatial light modulator based on Fourier transform," in *Proc. 2014 Conference on Lasers and Electro-Optics (CLEO)-Laser Science to Photonic Applications* (San Jose, CA, USA, Jun. 8–13, 2014), pp. 1–2.
5. U. Frisch, *Turbulence: The legacy of AN Kolmogorov* (Cambridge University Press, USA, 1995).
6. S. M. Ebstein, "Pseudo-random phase plates," Proc. SPIE **4493**, 150–155 (2002).
7. P. F. Almoro and S. G. Hanson, "Random phase plate for wavefront sensing via phase retrieval and a volume speckle field," Appl. Opt. **47**, 2979–2987 (2008).
8. J. Y. Joo, S. G. Han, J. H. Lee, H.-G. Rhee, J. Huh, K. Lee, and S. Y. Park, "Development and characterization of an atmospheric turbulence simulator using two rotating phase plates," Curr. Opt. Photonics **6**, 445–452 (2022).
9. R. Rampy, D. Gavel, D. Dillon, and S. Thomas, "Production of phase screens for simulation of atmospheric turbulence," Appl. Opt. **51**, 8769–8778 (2012).
10. N. Mordant, "Fourier analysis of wave turbulence in a thin elastic plate," Eur. Phys. J. B **76**, 537–545 (2010).
11. H. Zhai, B. Wang, J. Zhang, and A. Dang, "Fractal phase screen generation algorithm for atmospheric turbulence," Appl. Opt. **54**, 4023–4032 (2015).
12. K. Wang, X. Su, Z. Li, S. Wu, W. Zhou, R. Wang, S. Chen, and X. Wang, "Generation of non-Kolmogorov atmospheric turbulence phase screen using intrinsic embedding fractional Brownian motion method," Optik **207**, 164444 (2020).
13. C. Liu, S. Chen, X. Li, and H. Xian, "Performance evaluation of adaptive optics for atmospheric coherent laser communications," Opt. Express **22**, 15554–15563 (2014).
14. S. M. Jefferies, D. A. Hope, M. Hart, and J. Nagy, "High-resolution imaging through strong atmospheric turbulence and over wide fields-of-view," in *Proc. Advanced Maui Optical and Space Surveillance Technologies Conference* (Maui, Hawaii, USA, Sep. 10–13, 2013), id. E52.
15. C. Rao, L. Zhu, X. Rao, L. Zhang, H. Bao, L. Kong, Y. Guo, L. Zhong, X. Ma, M. Li, C. Wang, X. Zhang, X. Fan, D. Chen, Z. Feng, N. Gu, and Y. Liu, "Instrument description and performance evaluation of a high-order adaptive optics system for the 1 m new vacuum solar telescope at Fuxian Solar Observatory," Astrophys. J. **833**, 210 (2016).
16. M. C. Roggemann and B. M. Welsh, *Imaging Through Turbulence* (CRC press, USA, 1996).
17. J. W. Goodman, *Statistical Optics*, 2nd ed. (John Wiley & Sons, USA, 2015).
18. D. G. Stork, "Toward a signal-processing foundation for computational sensing and imaging: electro-optical basis and merit functions," APSIPA Trans. Signal Inf. Process. **6**, e8 (2017).
19. S. E. Troxel, B. M. Welsh, and M. C. Roggemann, "Off-axis optical transfer function calculations in an adaptive-optics system by means of a diffraction calculation for weak index fluctuations," J. Opt. Soc. Am. A **11**, 2100–2111 (1994).
20. R. J. Noll, "Zernike polynomials and atmospheric turbulence," J. Opt. Soc. Am. **66**, 207–211 (1976).
21. Thorlab, "WFS40-14AR Shack-Hartmann WFS, 11.26 mm Square Aperture, 300 μm Pitch, AR Coated MLA, 400 - 900 nm, Imperial Taps," (Thorlabs, Published date: Jul. 20, 2018), https://www.thorlabs.com/thorproduct.cfm?partnumber=WFS40-14AR&pn=WFS40-14AR;%2022 (Accessed Date: Sep. 12, 2022).
22. Artglory, "Crystal resin high opaque epoxy 1 kg," (Artglory), https://smartstore.naver.com/woorc/products/5251150069?NaPm=ct%3Dlwpqqzb4%7Cci%3D22d19ea56e0b2bf72b946b6c442b071c30ca7fa6%7Ctr%3Dsls%7Csn%3D377044%7Chk%3D4d46255dcd5526e87e1a87239bb9f31cdb25 (Accessed date: Aug. 24, 2023).
23. L. Catala, A. Ziad, Y. Fanteï-Caujolle, S. M. Crawford, D. A. H. Buckley, J. Borgnino, F. Blary, M. Nickola, and T. Pickering, "High-resolution altitude profiles of the atmospheric turbulence with PML at the Sutherland Observatory," Mon. Not. R. Astron. Soc. **467**, 3699–3711 (2017).
24. T. R. Rimmele and J. Marino, "Solar adaptive optics," Living Rev. Sol. Phys. **8**, 1–92 (2011).
25. D. L. Hutt and D. H. Tofsted, "Effect of atmospheric turbulence on propagation of ultraviolet radiation," Opt. Laser Technol. **32**, 39–48 (2000).